

High-precision broadband linear polarimetry of early-type binaries. V. The Binary System HD 165052 in Open Cluster NGC 6530^{*}

Yasir Abdul Qadir¹, Andrei V. Berdyugin¹, Vilppu Piirola¹, Takeshi Sakanoi²,
Masato Kagitani², and Svetlana V. Berdyugina^{3,4,5}

¹ Department of Physics and Astronomy, FI-20014 University of Turku, Finland
e-mail: yasir.abdulqadir@utu.fi

² Graduate School of Sciences, Tohoku University, Aoba-ku, 980-8578 Sendai, Japan

³ Istituto ricerche solari Aldo e Cele Daccó (IRSOL), Faculty of Informatics, Università della Svizzera italiana, Via Patocchi 57, Locarno, Switzerland

⁴ Euler Institute, Faculty of Informatics, Università della Svizzera italiana, Via la Santa 1, 6962 Lugano, Switzerland

⁵ Institut für Sonnenphysik (KIS), Georges-Köhler-Allee 401A, 79110 Freiburg, Germany

Received XX / Accepted XX

ABSTRACT

Aims. This is a continuation of our study of early-type binaries with high-precision broad-band polarimetry. This time, we are presenting results of our observations of the massive O+O-type binary system HD 165052 located in the very young open cluster NGC 6530. Our aim was to investigate the variations of linear polarization in this system with time and obtain independent estimate of orbital period from polarization data. By fitting phase-locked variations of Stokes parameters q and u , it is possible to obtain independent estimates of orbit inclination i , orientation Ω , and the direction of rotation.

Methods. We employed the Dipol-2 polarimeter in combination with the remotely controlled 60cm KVA and Tohoku T60 telescopes. Linear polarization measurements of HD 165052 were obtained in the B , V , and R passbands with an accuracy better than $\sim 0.01\%$. Lomb-Scargle method of period search was applied to the acquired polarization data to identify present periodic signals. To study interstellar polarization in NGC 6530, we observed 25 cluster stars located in close proximity to the binary.

Results. Our observations clearly revealed periodic variations of Stokes parameters in all three passbands with the amplitude $\sim 0.1\%$. Period search, applied to polarization data, detected unambiguous and strongest periodic signal at 1.47755 ± 0.005 d, that corresponds to half of the orbital period of 2.95510 ± 0.005 d. In the observed polarization variations, the second terms of the Fourier harmonics are clearly dominating suggesting that light scattering material is symmetrically distributed with respect to the orbital plane. We concluded that the most probable polarization mechanism is the electron scattering in the interacting stellar winds. We derived our best estimate of the orbital inclination i as $55^\circ + 5^\circ / -55^\circ$, and Ω as $148^\circ (328^\circ) + 20^\circ / -22^\circ$ averaged over B , V , and R passbands. Using the values of polarization variability amplitude, we estimated the mass-loss rate for the whole system to be $4.0 \times 10^{-7} M_\odot \text{ yr}^{-1}$. The direction of the binary system rotation on the plane of the sky is clockwise. Our observations of HD 165052 neighbour stars revealed complex behaviour of interstellar polarization in the cluster NGC 6530.

Key words. polarization – techniques: polarimetric – instrumentation: polarimeters – stars: individual: HD 165052 – binaries (including multiple): close – binaries: non-eclipsing

1. Introduction

Early-type binaries are massive and luminous binary stars with both companions of early B, or O spectral types. One of the key features of such binaries is that they often exhibit a noticeable amount of circum-binary material even if neither of the companions is filling its Roche lobe. This is occurring due to the extensive stellar winds. Interaction between these winds results in formation of hot bow shock area of the ionized gas between and around the companions. Light scattering on such gas may give rise to the variable linear polarization. Studying such polarization provides important information on the orbital parameters of the system and geometry / distribution of the

circum-binary material. We have been conducting polarimetric observations of early-type binaries using DiPol-2 polarimeter for about a decade from now. In our previous papers we have described results obtained for early-type binaries HD 48099 (Berdyugin et al. 2016), AO Cassiopeiae (Abdul Qadir et al. 2023a), and DH Cephei (Abdul Qadir et al. 2023b). In this paper we are presenting results of our polarimetric study of the early-type binary system HD 165052.

HD 165052 is a double-lined spectroscopic binary that consists of O7Vz primary star and O7.5Vz secondary star with a mass ratio $q = M_s/M_p = 0.91 \pm 0.01$ (Ferrero et al. 2013). The orbital period value determined in last ~ 20 years ranges from 2.95510d (Arias et al. 2002) to 2.95585d Rosu et al. (2023). Due to the noticeable eccentricity of orbit ($e = 0.09$) and clear presence of the apsidal motion in HD 165052, a number of detailed spectroscopic investigations have been conducted for this system in the past (e.g., Morrison & Conti

^{*} The polarization data for HD 165052 are only available in electronic form at the CDS via anonymous ftp to cdsarc.cds.unistra.fr (130.79.128.5) or via <https://cdsarc.cds.unistra.fr/cgi-bin/qcat?J/A+A/>

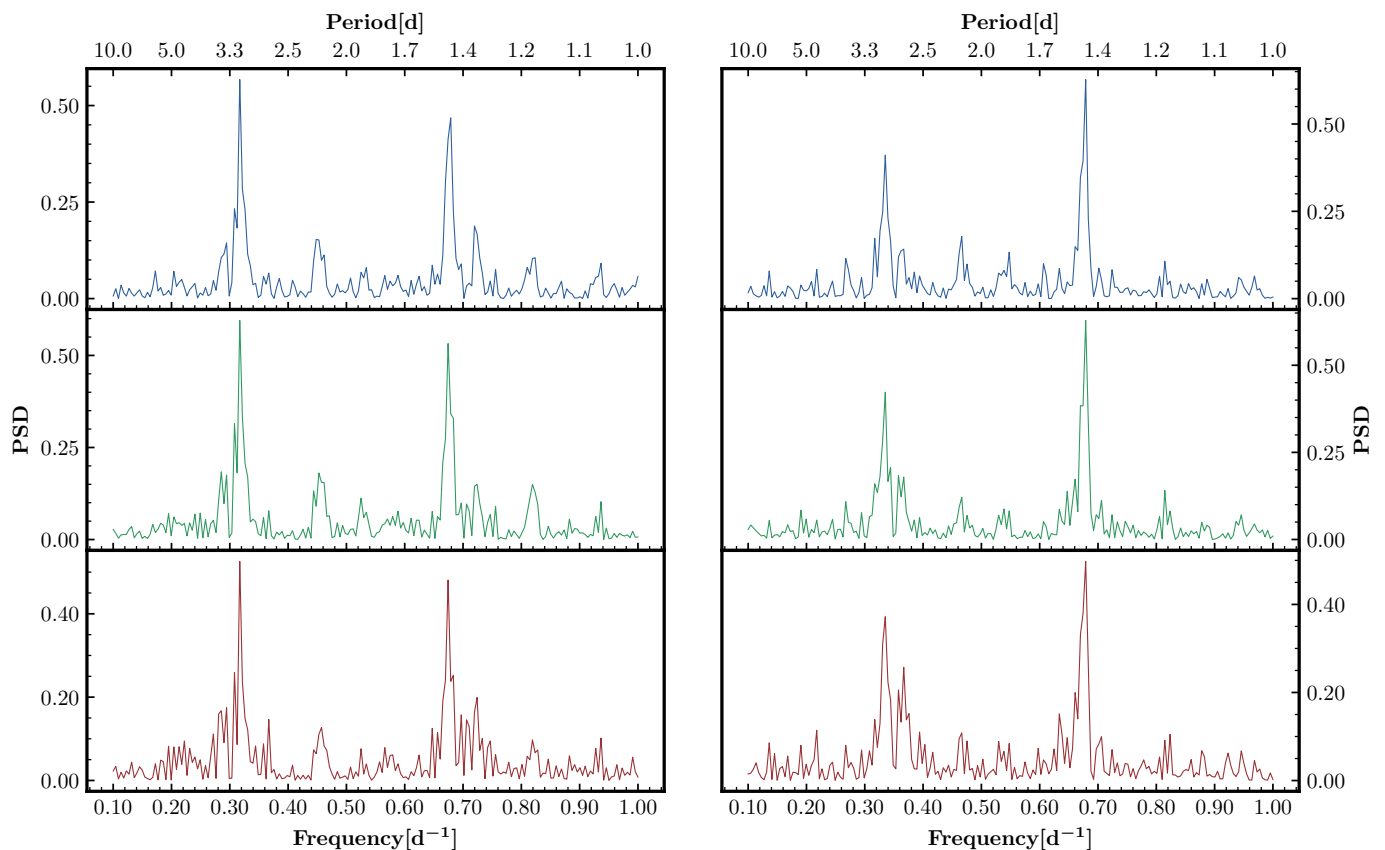


Fig. 1: Lomb-Scargle periodograms for Stokes q (left column) and u (right column) for HD 165052 obtained in the B , V , and R passbands (top, middle, and bottom panels respectively).

(1978); Stickland et al. (1997); Ferrero et al. (2013); Arias et al. (2002); Linder et al. (2007); Rosu et al. (2023)). HD 165052 belongs to the very young open cluster NGC 6530, which is a well studied cluster of our Galaxy because of its interesting history of star formation (e.g., Sung et al. (2000); Damiani et al. (2006); Topasna et al. (2020)).

As far as we know, no comprehensive polarization studies of HD 165052 and NGC 6530 have been undertaken in the past. Therefore, we carried out a series of precise broadband linear polarization observations of HD 165052 and measured linear polarization of its 24 nearby stars within NGC 6530 cluster. Our main goal was to detect potential orbital phase-locked variable linear polarization in the HD 165052. This allows to obtain independent estimates of its orbital parameters and study the distribution of circum-binary material. We emphasize that this goal can be achieved even if the exact amount of interstellar polarization component cannot be determined.

2. Polarimetric Observations

First polarization data set spanning over 32 nights was obtained in 2012 with the DiPol-2 (Piirola et al. 2014) polarimeter on the 60cm KVA telescope at the Observatorio Roque de los Muchachos (La Palma, Canary Islands). In 2015 and 2016, we gathered another sets of data that spanned over 9 nights and 4 nights subsequently with the same polarimeter on the 60cm Tohoku T60 telescope at Haleakalā Observatory (Hawaii). Finally, a last set of data, spanning over 23 nights, was acquired with the T60 telescope in 2023. In the year 2023, 24 field stars,

members of NGC 6530 cluster in the vicinity of HD 165052 were also observed. All our polarimetric observations were conducted in the B , V , and R passbands simultaneously in remote mode. For HD 165052, we usually obtained 256 images with an exposure time of 10 s per each night, which yielded 64 measurements of the Stokes q and u parameters. Corresponding observational log is given in Table A.1.

The process of data reduction involved standard calibration, including bias and dark frame subtraction. Correction for flat-field effects is also done, although this correction does not impact final results significantly. Normalized Stokes q and u parameters were derived from flux intensity ratios of orthogonally polarized stellar images $Q_i = I_e(i)/I_o(i)$, obtained at orientations of half-wave plate $i = 0.0^\circ, 22.5^\circ, 45.0^\circ, 67.5^\circ, \dots, 337.5^\circ$. More details can be found in Piirola et al. (2020) and Abdul Qadir et al. (2023a).

To determine instrumental polarization, we observed about two dozen non-polarized standard stars. The instrumental polarization for both telescopes in the B , V , and R bands ranged from 0.004% to 0.006%, determined with the accuracy of 0.0002% – 0.0003%. Highly polarized standard stars HD 204827 and HD 25443 were used to calibrate the polarization angle zero-point (see Table A.2 for their polarization degrees and angles). The errors of the nightly average polarization measurements for T60 are from 0.001% to 0.004% in the B and R bands and from 0.002% to 0.006% in the V band. For the data obtained with the KVA, the errors are somewhat larger, and are in the range from 0.006% to 0.015%.

Table 1: FAPs for the real and alias periods obtained for HD 165052 from period search.

	Filter	Period[d]	FAP
Stokes q :	B	1.47755	8.5×10^{-24}
		3.07101	3.9×10^{-18}
	V	1.47756	6.7×10^{-22}
		3.07096	2.8×10^{-18}
R	1.47757	1.7×10^{-18}	
	3.07093	9.3×10^{-16}	
Stokes u :	B	1.47754	2.5×10^{-24}
		3.07108	2.3×10^{-18}
	V	1.47755	2.3×10^{-19}
		3.07105	1.4×10^{-14}
	R	1.47754	4.5×10^{-19}
		3.07105	4.8×10^{-15}

3. Data Analysis

3.1. Period Search

To search for periodic signals in our polarimetric data, we employed Lomb-Scargle algorithm (Lomb 1976; Scargle 1982). The benefit of using Lomb-Scargle algorithm is that it uses the least squares method to fit sinusoidal on unevenly sampled data, which it is often the case with astronomical data. To execute Lomb-Scargle algorithm with `PYTHON` code, we used package from `astropy.timeseries`¹ (Price-Whelan et al. 2018).

The variations of Stokes parameters of polarization arising from the scattered light in the binary system with (near) circular orbit typically show two maxima and minima per orbital period separated by 0.5 in the orbital phase (Brown et al. 1978). Therefore, Lomb-Scargle algorithm applied to binary polarization data, is expected to detect *half* of the orbital period. We have plotted Lomb-Scargle periodograms for both Stokes q and u in B , V , and R passbands in Figure 1.

As it was expected, Lomb-Scargle algorithm has detected half of the orbital period, $P_{\text{orb}/2}$, with a well-constrained error of $\sigma_{\text{orb}/2}$. While the full orbital period, $P_{\text{orb}} = 2 \times P_{\text{orb}/2}$, the errors on P_{orb} should remain equivalent to that of $P_{\text{orb}/2}$, i.e., $\sigma_{\text{orb}} = \sigma_{\text{orb}/2}$. For Stokes q , we found the best orbital periods as $P_{\text{orb}} = 2.95510 \pm 0.006$ d, 2.95512 ± 0.007 d, and 2.95514 ± 0.008 d in the B , V , and R passbands respectively. Likewise, for Stokes u , we found the best periods as $P_{\text{orb}} = 2.95508 \pm 0.006$ d, 2.95510 ± 0.007 d, and 2.95508 ± 0.008 d. Thus, the derived average value over Stokes q and u and across all passbands is $P_{\text{orb}} = 2.95510 \pm 0.005$ d. The errors on the periods were calculated using corresponding power values and measurement uncertainties of the frequencies related to orbital period peaks given in Table 1. These frequency errors were then converted to days using the relationship $\Delta P = \Delta f / f^2$.

Moreover, we do notice the presence of strong alias peak at ~ 3.1 d (frequency ~ 0.32 d⁻¹) in all periodograms. An alias peak related to real period can appear when the frequency of the that period is not less than half of the sampling frequency, i.e., Nyquist frequency (f_{ny}). In such a situation, two waves are produced that differ by $1/f_{\text{ny}}$. The (half) orbital period for HD 165052, ~ 1.47755 d is at frequency of ~ 0.68 d⁻¹, which is more than half of our sampling frequency. Therefore, alias peaks can be expected at around $1/(1-1/1.47755) = 3.094$ d or at frequency close to ~ 0.323 d⁻¹. As one can see, the alias peaks which are

¹ <https://docs.astropy.org/en/stable/timeseries/lombscargle.html>

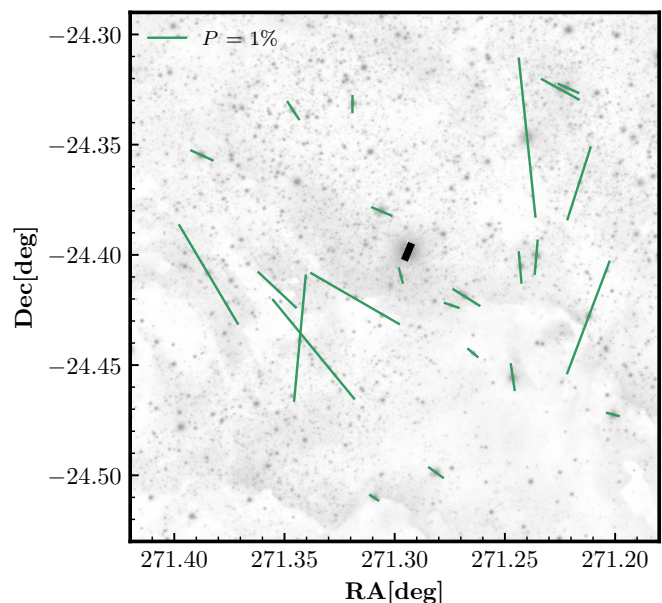


Fig. 2: Interstellar polarization map in the vicinity of HD 165052. Measurements made in the V passband are presented. Binary is in the center of the field and its average value of polarization shown with thicker black line. The length of bars corresponds to the degree of linear polarization P , and the direction corresponds to the polarization angle (measured from the north to the east).

quite close to that frequency indeed present in our periodograms (cf. Shannon (1949); VanderPlas (2018)). It is not uncommon to observe such alias peaks in Lomb-Scargle periodograms of astronomical data (e.g., Kosenkov & Vvedina (2018); Abdul Qadir et al. (2023a); Abdul Qadir et al. (2023b)).

Furthermore, we calculated False Alarm Probability (FAP) for (half) orbital period of HD 165052, and its alias peaks using bootstrap method (Suveges 2012). FAP values of both real and alias peaks in B , V , and R passbands for both Stokes q , and u are given in Table 1. The FAP values for both orbital peaks and alias peaks are very low, because the algorithm can not distinguish between them. The value of true orbital period derived from our polarization data is very close to the values of 2.95510d derived by Arias et al. (2002) and 2.95515 d derived by Linder et al. (2007). As we have found, the longer value of orbital period 2.95585 d, obtained recently by Rosu et al. (2023) cannot be used to provide an adequate fit to observed variability of our polarization data. Thus, our independent period search, performed on polarization data, provides support for the previously measured shorter value of the orbital period in HD 165052. We did not detect presence of any other (real) periodic signal in polarimetric data except for the orbital.

3.2. Interstellar Polarization

HD 165052, being a rather distant binary system with a parallax of 0.7893 ± 0.0297 mas (Gaia Collaboration et al. 2021), is expected to exhibit interstellar (IS) polarization component due to the presence of interstellar dust along the line of sight. In addition, one can expect a significant contribution to the IS polarization from the dust which presents in the young stellar cluster NGC 6530. We have attempted to quantify the IS component of polarization in HD 165052 by conducting polarization observations of 24 field stars located in the vicinity

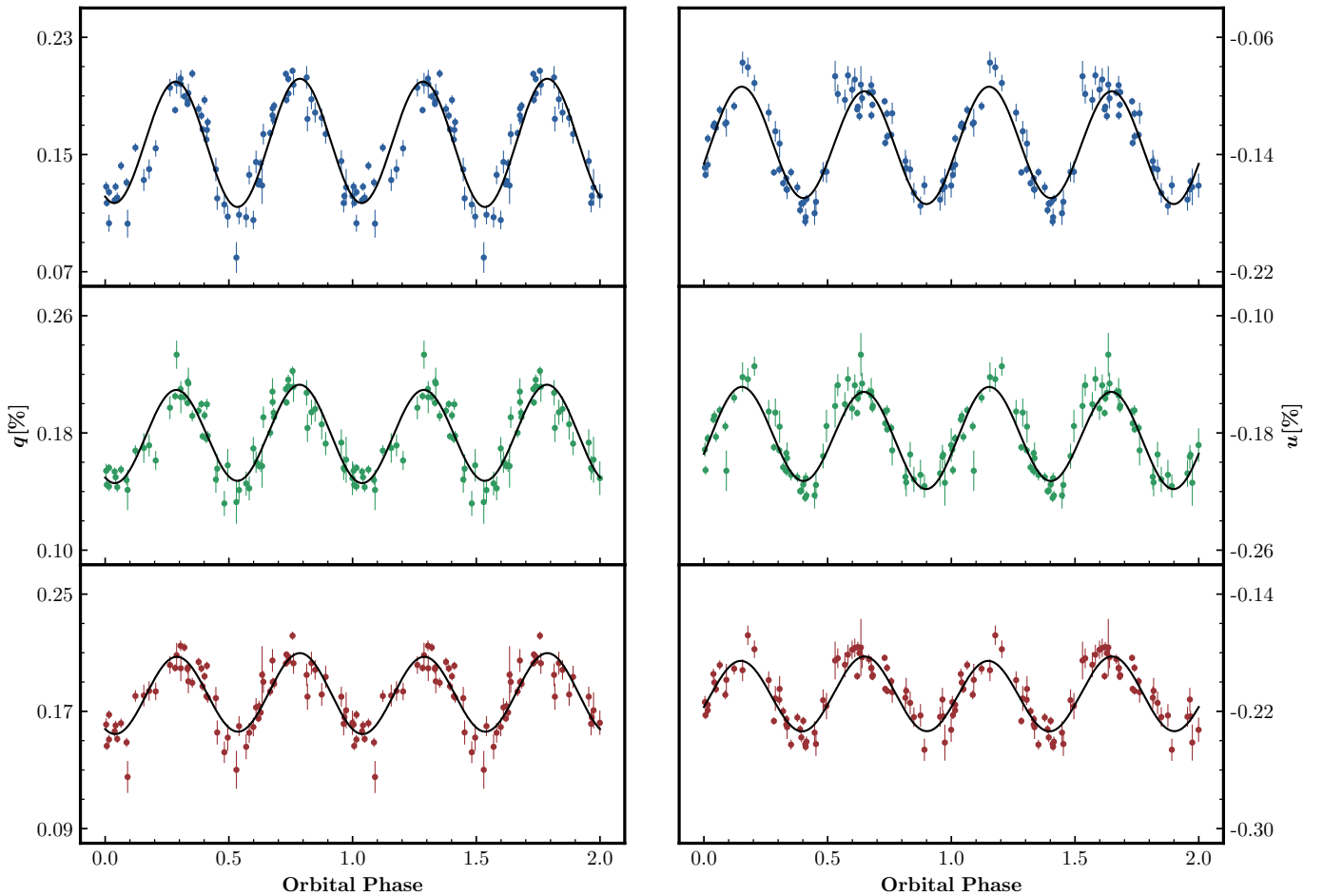


Fig. 3: The variability of observed Stokes parameters q and u for HD 165052 in the B , V , and R passbands (top, middle, and bottom panels respectively), phase-folded with the orbital period of 2.95510d. Fourier fit curves (see Sect. 3.3) are shown with solid lines, and the best fit Fourier coefficients are given in Table 2. The lengths of the bars correspond to $\pm\sigma$ errors.

Table 2: Best fit Fourier coefficients for Stokes q and u .

Filter	q_0	q_1	q_2	q_3	q_4	u_0	u_1	u_2	u_3	u_4
B	0.1581	0.0015	-0.0007	-0.0384	-0.0185	-0.1335	-0.0007	0.0025	-0.0121	0.0363
	± 0.0016	± 0.0021	± 0.0028	± 0.0022	± 0.0023	± 0.0013	± 0.0022	± 0.0021	± 0.0022	± 0.0020
V	0.1788	-0.0004	-0.0019	-0.0289	-0.0143	-0.1829	-0.0012	0.0030	-0.0101	0.0310
	± 0.0012	± 0.0017	± 0.0021	± 0.0020	± 0.0020	± 0.0011	± 0.0019	± 0.0017	± 0.0018	± 0.0017
R	0.1819	-0.0005	-0.0014	-0.0235	-0.0123	-0.2088	-0.0008	-0.0012	-0.0074	0.0236
	± 0.0010	± 0.0015	± 0.0018	± 0.0016	± 0.0016	± 0.0012	± 0.0018	± 0.0019	± 0.0017	± 0.0018

of HD 165052. Results of these observations are presented in Table A.3. For each star, we give its Gaia DR3 identifier (Gaia Collaboration et al. 2021), coordinates, parallax, polarization degree, polarization angle, and the total number of polarization measurements in the three passbands.

Figure 2 illustrates the polarization map of NGC 6530, showing a significant scatter in both polarization degrees (ranging from 0.07% to 4.15%) and polarization angles (ranging from 2° to 176°) for the observed field stars, despite the fact that they all have parallaxes within the range of ~ 0.3 mas. This variation in polarization properties among the cluster stars, including those closest to HD 165052, indicates that the IS polarization in NGC 6530 is strongly not uniform. Consequently, polarization data for the observed field stars

cannot help us in accurate determination of IS polarization component for HD 165052 itself.

The presence of significant scatter in the polarization properties of stars within the NGC 6530 suggests that the region is dynamically complex, with varying distribution of interstellar dust and directions of interstellar magnetic field. This behavior is typical for a young open clusters, where stars are still forming and interacting with their surroundings. As a result, one can expect rather complex and strongly not uniform distribution of dust on the different lines of sight within the cluster. For stars 7, 20, 21, and 22, the minimum degree of polarization is in the V passband which is not typical for the IS polarization produced by homogeneous diffuse interstellar dust. We can suggest that in addition to variations in dust particles orientation and density, the variations in particles size and composition may also occur

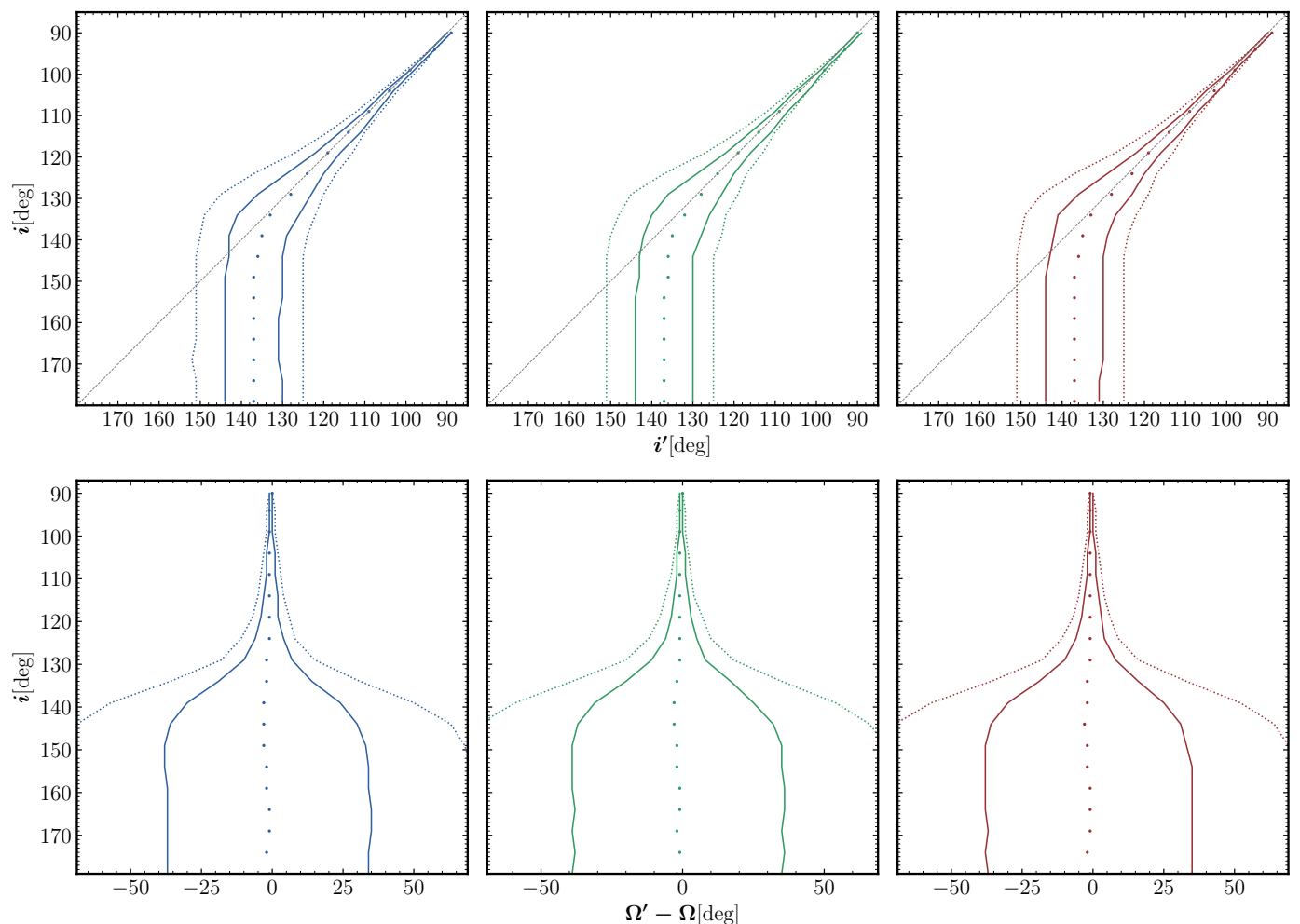


Fig. 4: Confidence intervals (solid lines for $\pm 1\sigma$, and dotted lines for $\pm 2\sigma$) of i (upper panels), and Ω (lower panels) for γ values of 316, 265, and 222 for the B , V , and R passbands (left, middle, and right panels respectively). The dotted lines in upper panels illustrate critical values of i . Note, that the inclination range of $180^\circ - 90^\circ$ shown on the plots is fully equivalent to $0^\circ - 90^\circ$. If the orbital rotation as seen on the plane of the sky is clockwise, the BME method yields inclination value between 90° and 180° .

in the NGS 6530. We cannot also exclude that some of the field stars are intrinsically polarized. The most suspicious is the star 23 that shows sharp increase of polarization toward near infrared, e.g. from nearly zero value in the B-band to more than 1.0% in the R-band.

Although we were not able to estimate the value of IS polarization component for the HD 165052, we hope that our polarimetric observations of field stars provide insights into the structure and properties of the interstellar medium in the NGS 6530. The polarization data collected from field stars near HD 165052 can be used in future studies for examinations and modeling of the dynamic interaction between the interstellar dust, magnetic fields, and stellar community in the NGC 6530.

3.3. Periodic Polarization Variability and Orbital Parameters

We used standard analytical method based on two-harmonics Fourier fit (commonly known as BME approach (Brown et al. 1978)) to fit the phase-folded curves of the Stokes q and u parameters. This method assumes a circular orbit with co-rotating light scattering envelope and the fit includes zeroth, first and second harmonics terms:

$$\begin{aligned} q &= q_0 + q_1 \cos \lambda + q_2 \sin \lambda + q_3 \cos 2\lambda + q_4 \sin 2\lambda, \\ u &= u_0 + u_1 \cos \lambda + q_2 \sin \lambda + q_3 \cos 2\lambda + q_4 \sin 2\lambda, \end{aligned} \quad (1)$$

where $\lambda = 2\pi\phi$, and ϕ represents the phase of the orbital period. The polarimetric data of Stokes q and u were phase-folded using the orbital period P_{orb} [d] = 2.95510 and T_0 [HJD] = 2449871.75 from Arias et al. (2002). This was an obvious choice, because the value of P_{orb} obtained by Arias et al. (2002) is very close to that derived by us. Folding polarization data with the new value $P_{\text{orb}} = 2.95585\text{d}$ obtained by (Rosu et al. 2023) revealed that it fails to represent adequately periodic variability of our polarization data set.

Bayesian inference method was employed to fit the model to the data points (Hogg & Foreman-Mackey 2018). Using this method on Stokes q and u data for the B , V , and R passbands, we determined the optimal Fourier coefficients. Subsequently, we performed curve fitting of the observed polarization data, as shown in Figure 3. The fit reveals an amplitude of variability of $\sim 0.10\%$, accompanied by some non-periodic scatter. We used `curve_fit` function of the `scipy.optimize`² library in

² <https://docs.scipy.org/doc/scipy/reference/optimize.html>

Table 3: Orbital parameters for HD 165052 derived from the polarization measurements in the B , V , and R passbands. Parameters A_q and A_u are computed with Eq. B.4.

Filter	$i^{(a,b)}$	$\Omega^{(b)}$	A_q/A_u
B	$125^\circ - 5^\circ / +55^\circ$ ($55^\circ + 5^\circ / -55^\circ$)	$155^\circ + 34^\circ / -37^\circ$ ($335^\circ + 34^\circ / -37^\circ$)	21.7/20.3
V	$126^\circ - 5^\circ / +54^\circ$ ($54^\circ + 5^\circ / -54^\circ$)	$133^\circ + 35^\circ / -38^\circ$ ($313^\circ + 35^\circ / -38^\circ$)	18.3/10.6
R	$123^\circ - 5^\circ / +57^\circ$ ($57^\circ + 5^\circ / -57^\circ$)	$146^\circ + 35^\circ / -37^\circ$ ($336^\circ + 35^\circ / -37^\circ$)	17.9/21.8

Notes. ^(a) These are de-biased values. The derived values through optimal Fourier coefficients, are $124^\circ(56^\circ)$, $125^\circ(55^\circ)$, and $122^\circ(58^\circ)$ in the B , V , and R passbands, respectively. ^(b) The given confidence intervals correspond to $\pm\sigma$.

PYTHON to determine values of Fourier coefficients that were used as initial guess (priors) for our Bayesian interface, which enhanced the precision and subsequent values are given in Table 2.

The orbital inclination i and orbit's orientation in the sky, represented by the longitude of the ascending node Ω can be derived from the first ($q_{1,2}$, $u_{1,2}$) and second ($q_{3,4}$, $u_{3,4}$) harmonic terms of the Fourier series. Complete set of equations for computing orbital and other parameters are presented by Drissen et al. (1986). For additional details, please refer to Appendix B. However, in cases where the orbit is circular or nearly circular, and the distribution of scattering material is symmetric with respect to the orbital plane, the influence of the first harmonic terms becomes negligible. As is seen from Table 2, this a clear case for HD 165052. Small orbit eccentricity has a very little / no effect on the fit which is dominated by second harmonics. Thus, we have used only the second harmonic terms for deriving orbital parameters from the Fourier coefficients obtained for each passband.

The parameters A_q and A_u are the amplitude ratios between the second and first harmonics of Stokes q and u , respectively. These parameters are quantifying the degree of a symmetry and concentration of scattering material around the orbital plane for a circular orbit. Expressions for computing these parameters are given in Appendix B.

By applying Equations (B.1 – B.5) from Appendix B, we computed the values of i , Ω , A_q , and A_u for the B , V , and R passbands. Results are shown in Table 3. The large values of A_q and A_u for all passbands indicate high degree of symmetry and/or concentration of light scattering material toward orbital plane in HD 165052.

As is evident from Figure 3, there is a noticeable non-periodic scatter around the fitting curves in all passbands. Moreover, because HD 165052 is a non-eclipsing system, the true inclination should be small. Thus, we should expect pronounced bias, asymmetric confidence intervals for the derived inclination i , and broad confidence intervals for Ω .

To determine the bias and corresponding confidence intervals for i and Ω we have used a "figure of merit" parameter γ , introduced and defined by Wolinski & Dolan (1994) as:

$$\gamma = \left(\frac{A}{\sigma_p} \right)^2 \frac{N}{2}, \quad (2)$$

where, A is the periodic fraction of the amplitude of polarization variability measured from the best fit and defined

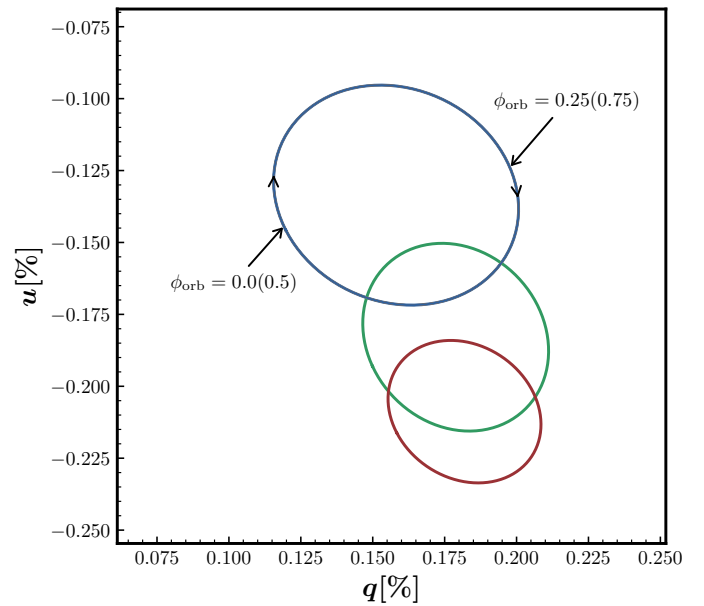


Fig. 5: The variability of observed polarization for HD 165052 plotted on the Stokes (q , u) plane, represented by the ellipses of second harmonics of Fourier fit. Blue, green, and red colors represent B , V , and R passbands respectively. The clockwise direction and phases of the orbital period are shown for the B band ellipse. The angle between the major axis and the q -axis gives the orientation Ω .

as:

$$A = \frac{|q_{\max} - q_{\min}| + |u_{\max} - u_{\min}|}{4}, \quad (3)$$

σ_p is a standard deviation that is determined from the scatter of the observed Stokes parameters around the best fit curves, N is the number of observations, and q_{\max} , q_{\min} , u_{\max} , u_{\min} are maximum and minimum values of the fitted Stokes parameters q and u . With our values of $\sigma_p = 0.013$, 0.011 , 0.010 we have derived the corresponding values of $\gamma = 316$, 265 , 222 for the B , V , and R passbands respectively.

Due to the noise that unavoidably presents in real polarimetric data, the value of i derived from Fourier fits consistently exhibits a bias towards higher values (Aspin et al. (1981); Simmons et al. (1982); Wolinski & Dolan (1994)). The extent of this bias depends not only on the amplitude of noise, but also on the true value of the inclination. Lower true value of i leads to a more pronounced bias. A similar bias towards higher values can also be introduced by *real* non-periodic fluctuations in polarization (Manset & Bastien 2000). Moreover, as it was shown by Manset & Bastien (2000), for low eccentricity orbit, BME method can yield the realistic inclination only when its true value of $i > 45^\circ$. This bias also leads to asymmetry of 1σ and 2σ confidence intervals for i , which stretch unevenly, with the lower boundary extending towards *lower* i values. In the case when inclination is low (typical for non-eclipsing systems like HD 165052) and small value of merit parameter γ (defined by Eq. 2), the lower limit of the confidence interval extends down to $i = 0^\circ$. In such instances, polarimetric data can only provide an upper limit for the true inclination value. Furthermore, the range of Ω confidence intervals expands rapidly as the true inclination decreases (Wolinski & Dolan 1994).

Using these values of γ and N number of our data points with their corresponding orbital phases and measurements

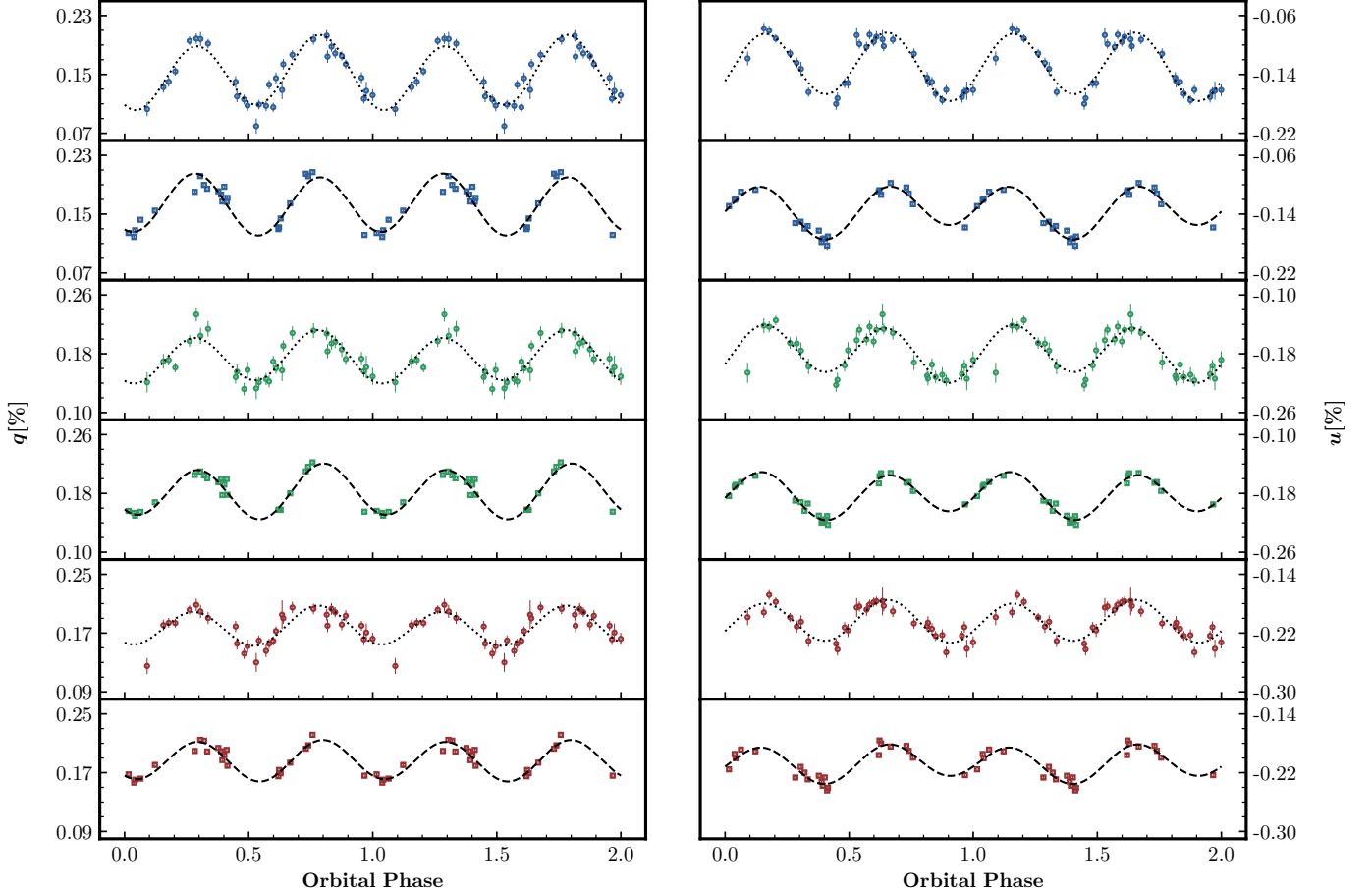


Fig. 6: The variability of observed Stokes parameters q and u for HD 165052 in the B , V , and R passbands (top two, middle two, and bottom two panels respectively), phase-folded with the orbital period of 2.95510d. The dotted Fourier fit curves and data points represented with circles show the data obtained in 2012; dashed Fourier fit curves and data points represented with squares show the data obtained in 2023. Best fit Fourier coefficients for two datasets are given in Table 4. The lengths of the bars correspond to $\pm\sigma$ errors.

Table 4: Best fit Fourier coefficients for Stokes q and u for data obtained in 2012 (upper panel) and 2023 (lower panel).

Filter	q_0	q_1	q_2	q_3	q_4	u_0	u_1	u_2	u_3	u_4
B	0.1506	-0.0016	-0.0084	-0.0402	-0.0210	-0.1277	-0.0043	0.0019	-0.0169	0.0403
	± 0.0024	± 0.0030	± 0.0035	± 0.0035	± 0.0032	± 0.0019	± 0.0030	± 0.0027	± 0.0028	± 0.0028
V	0.1743	-0.0011	-0.0057	-0.0300	-0.0124	-0.1777	-0.0047	0.0062	-0.0116	0.0325
	± 0.0025	± 0.0035	± 0.0040	± 0.0039	± 0.0034	± 0.0022	± 0.0032	± 0.0027	± 0.0031	± 0.0033
R	0.1783	0.0017	-0.0041	-0.0230	-0.0087	-0.2046	-0.0025	-0.0013	-0.0103	0.0252
	± 0.0018	± 0.0026	± 0.0023	± 0.0025	± 0.0025	± 0.0016	± 0.0024	± 0.0025	± 0.0022	± 0.0023
B	0.1630	0.0018	0.0030	-0.0357	-0.0172	-0.1339	0.0080	-0.0058	-0.0106	0.0289
	± 0.0025	± 0.0040	± 0.0049	± 0.0049	± 0.0045	± 0.0013	± 0.0022	± 0.0023	± 0.0021	± 0.0021
V	0.1820	0.0042	-0.0033	-0.0280	-0.0196	-0.1818	0.0063	-0.0015	-0.0106	0.0264
	± 0.0017	± 0.0028	± 0.0030	± 0.0028	± 0.0029	± 0.0010	± 0.0017	± 0.0018	± 0.0016	± 0.0019
R	0.1863	0.0019	-0.0008	-0.0224	-0.0148	-0.2069	0.0033	-0.0049	-0.0082	0.0216
	± 0.0016	± 0.0026	± 0.0029	± 0.0027	± 0.0027	± 0.0017	± 0.0027	± 0.0030	± 0.0028	± 0.0026

errors, we performed our own Monte Carlo simulations to determine 1σ and 2σ confidence intervals for i and Ω (see Figure 4) by following the methodology described by Wolinski & Dolan (1994). We modeled Stokes parameters for values of i ranging from 180° to 90° with a decreasing step of 5° using the standard Brown et al. (1978) model (Eq. 1). This inclination range is fully equivalent to the "normal" range of $0^\circ - 90^\circ$ and reflects the fact that orbital rotation in HD 165052 binary

system is clockwise. Then, we simulated the Gaussian noise in Stokes q and u by adding the fluctuations of the variance $\sigma^2 = 0.5NA^2/\gamma$. The Fourier model (Eq. 1) was then fit to the simulated data using the Bayesian approach identical to the one that we used to derive Fourier coefficients given in Table 2. Then, using derived Fourier coefficients of simulated data, we derived inclination i' using Eq. B.1. For confidence intervals on Ω , we determined $\Omega' - \Omega$, where Ω' is deduced using Eq. B.2,

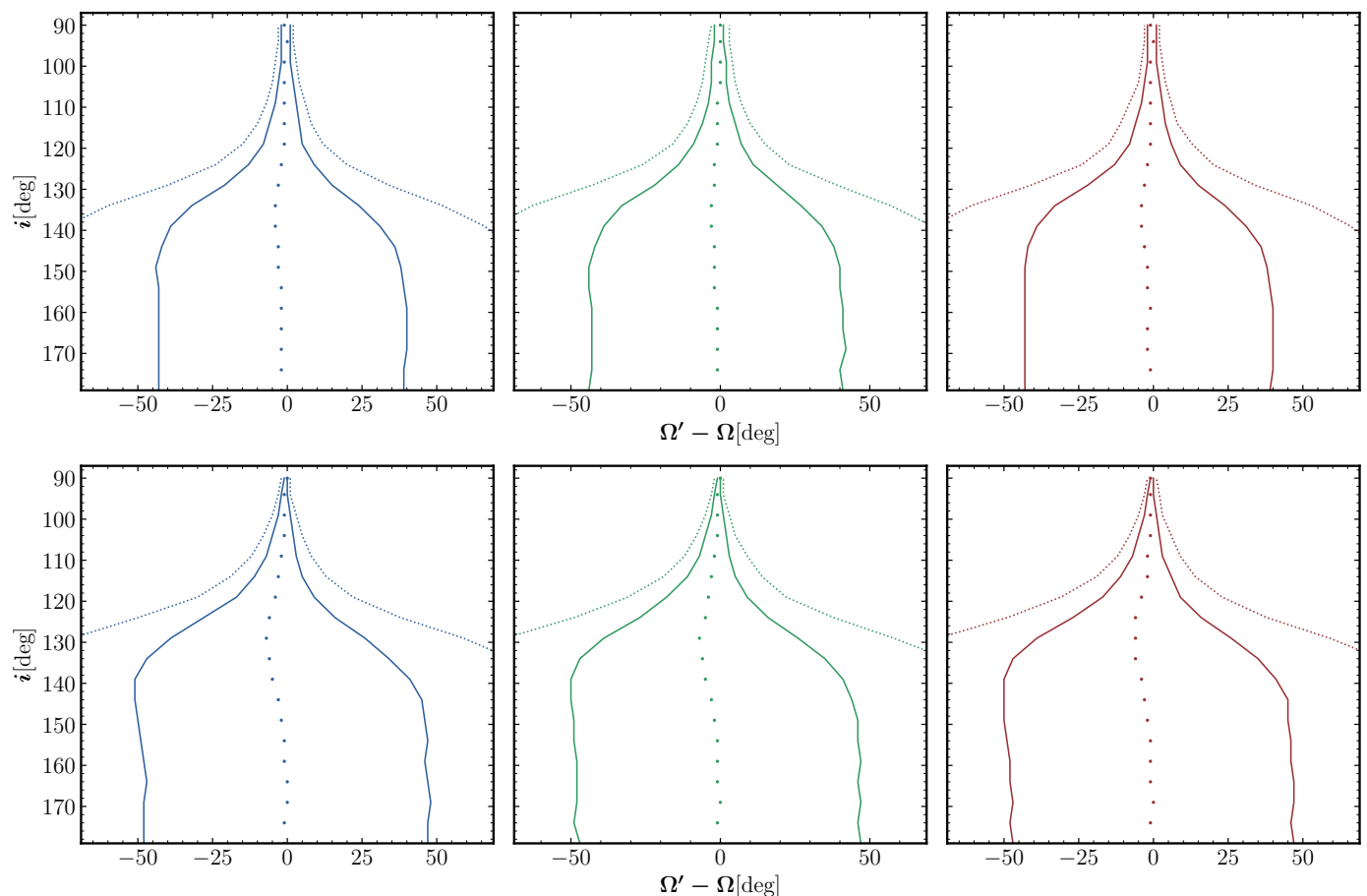


Fig. 7: Confidence intervals (solid lines for $\pm 1\sigma$, and dotted lines for $\pm 2\sigma$) of Ω' for 2012 dataset (upper panels) with γ values of 185, 70, and 72 for the *B*, *V*, and *R* passbands (left, middle, and right panels respectively), and for 2023 dataset (lower panels) with γ values of 145, 240, and 171 for the *B*, *V*, and *R* passbands (left, middle, and right panels respectively). Note, that confidence intervals for season 2012 are somewhat narrower due to the larger number of data points and, therefore, better phase coverage.

and for simplicity, we chose the input value $\Omega = 0$. For each input value of i , we obtained 100 values of i' , and $\Omega' - \Omega$.

Our confidence intervals shown on Figure 4, when compared to those presented by Wolinski & Dolan (1994), tend to be narrower for the similar values of γ . This difference arises from *larger* number of observations $N = 68$ in our case, in comparison with $N = 23$ used by Wolinski & Dolan (1994). A larger value of N provides better phase coverage and thus makes confidence intervals narrower. While γ reflects the precision of the Fourier fit, *phase sampling* factor also contributes to the width of confidence intervals. Thus, increasing N increases density of phase sampling and decreases width of confidence intervals, even for the smaller values of γ . The small asymmetry in our confidence intervals can be attributed to the uneven phase sampling (typical for real observations) as compared to even phase coverage employed by Wolinski & Dolan (1994).

Our derived inclinations for all passbands (see Table 3) are close to the critical value of i plotted on Figure 4. Beyond this threshold, the lower limit of 1σ confidence interval extends to $i = 180^\circ$ (or $i = 0^\circ$), see Wolinski & Dolan (1994). This implies that with our polarization data analysis, we can only establish an upper boundary $i \simeq 55^\circ$ on the orbit inclination in HD 165052.

To determine confidence intervals for Ω , we have set the true inclination angle $i = 22.5^\circ$, as determined by Rosu et al. (2023). As we believe, this estimate, based on analysis of spectroscopy data and atmospheric models is much better in comparison with

polarimetrically derived i . O-type stars typically have the masses exceeding $20 M_\odot$. The values of $M \sin^3 i$ derived by Rosu et al. (2023) and others from spectroscopy are noticeably low, within the range of $1.24 M_\odot - 1.37 M_\odot$, implying that inclinations higher than 23.1° would result in masses below the $20 M_\odot$ threshold. The confidence intervals for Ω derived in this way are given in Table 3. As one can see, despite large errors, the values of Ω obtained for different wavelengths are in good agreement and the average angle Ω of orbit orientations on the plane of sky is $\sim 145^\circ$ ($\sim 325^\circ$). Note, that there is an inherited ambiguity $\pm 180^\circ$ for Ω determined from the polarization data. The values provided in Table 3 are reflecting this.

Figure 5 shows ellipses of the second harmonics on the (q, u) plane for the *B*, *V*, and *R* passbands. The degree of eccentricity of these ellipses is linked to the orbital inclination i , while the orientation of their major semi-axes in relation to the q -axis gives the orientation of the orbit Ω on the sky plane. The direction of the ellipse traversal mirrors the orbital motion direction on the celestial plane. Given the derived inclination range of $90^\circ \leq i \leq 180^\circ$, the binary system rotation on plane of the sky occurs clockwise.

Table 5: Orbital parameter Ω for HD 165052 derived for the B , V , and R passbands. The upper panel values are obtained for dataset from year 2012 and the lower panel values are from year 2023.

Filter	$\Omega^{(a)}$
B	$328^\circ (148^\circ) + 39^\circ / -43^\circ$
V	$283^\circ (103^\circ) + 41^\circ / -44^\circ$
R	$258^\circ (78^\circ) + 40^\circ / -43^\circ$
B	$170^\circ (350^\circ) + 47^\circ / -48^\circ$
V	$154^\circ (334^\circ) + 47^\circ / -49^\circ$
R	$152^\circ (332^\circ) + 47^\circ / -47^\circ$

Notes. ^(a) The given confidence intervals correspond to $\pm\sigma$.

3.4. Effect of the Apsidal Motion

HD 165052 has been known to exhibit apsidal precession (Arias et al. (2002); Ferrero et al. (2013); Rosu et al. (2023)) that can be utilized for confirming the predictions of general relativity theory, as the system's high mass and proximity make relativistic effects more pronounced. Ferrero et al. (2013) determined the apsidal motion rate of the system to be $12.1 \pm 0.3 \text{ yr}^{-1}$ and recently Rosu et al. (2023) derived the value of $11.3 + 0.64 / - 0.49 \text{ yr}^{-1}$.

We benefit from our extensive polarimetric observational history of HD 165052, spanning nearly 11 years. Our dataset comprises 33 data points acquired from the KVA telescope in 2012 and an additional 23 data points collected from the T60 telescope in 2023 (Table A.1). To investigate possible effect of apsidal motion through polarimetry, we conducted separate Fourier fits on these two datasets. Best fits are shown on Figure 6 and the corresponding Fourier coefficients are presented in Table 4. As is seen from Table 4, the effect of apsidal motion on the polarization variability, if present, appears to be very subtle. Only for Stokes u in the B-band the difference in Fourier term u_4 between two datasets is larger than 3σ . The presence of non-periodic noise in both fits is also obvious.

Nevertheless, we have tried to derive the separate values of Ω for two sets of polarization data in order to estimate the significance of the difference between them. For estimation of confidence intervals for the values of Ω we have employed the method described in the previous section. The corresponding 1σ and 2σ confidence intervals are shown on Figure 7. The resulting values of Ω are presented in Table 5. As is seen from Figure 7, 2σ confidence intervals for derived Ω for the orbit inclination i above 135° (or below 45°) are extending up to $(-180^\circ, +180^\circ)$. Thus, although analysis of our polarization data do show some evidence for the apsidal motion, we cannot reliably estimate its rate due to large uncertainty in value of Ω derived from our polarization data.

3.5. Determination of the mass-loss rate

Because HD 165052 is an O-type binary, the most likely cause for the polarization variations is the electron scattering in the stellar winds of the hot components. The strong evidence for presence of the hot shocked gas region due to wind-to-wind interaction in HD 165052 was already presented by Arias et al. (2002) from their analysis of ROSAT data. The presence of a real stochastic variability in polarization of HD 165052 is also quite obvious. The natural explanation for this phenomenon is highly clumped radiatively driven stellar winds which is not uncommon in early-type binaries consisting of O-type components.

It is possible to estimate mass-loss rate from the component(s) in early-type binary from polarization variability amplitude employing the method proposed by St. -Louis et al. (1988). The method uses the polarization variability amplitude A_p defined in Brown et al. (1978) as:

$$A_p = \tau_o H (1 + \cos^2 i), \quad (4)$$

where, the moment $\tau_o H$ can be calculated from formula B.6. The values of A_p determined from our Fourier fits are 0.059%, 0.046%, and 0.039% for the B , V , and R passbands, respectively. Although electron scattering is independent of wavelength and should yield equal amplitudes, the differences, however, may arise from dilution effects caused by unpolarized radiation from the gaseous disk / envelop. As it was shown by St. -Louis et al. (1988), one can estimate the mass-loss rate due to stellar wind from the primary component with the following formula:

$$A_p = \frac{(1 + \cos^2 i) 3\sigma_t f_c \dot{M}}{(16\pi)^2 m_p v_\infty a} I, \quad (5)$$

Here, \dot{M} signifies mass-loss rate, f_c denotes the fraction of total light from the companion star, v_∞ stands for wind terminal velocity, a represents semi-major axis, and I is an integral. The evaluation of this integral requires selection of a specific wind velocity law, characterized by the parameter β . Thus, we can re-write Equation 5 as follows:

$$\dot{M} = \frac{(16\pi)^2 m_p v_\infty a A_p}{(1 + \cos^2 i) 3\sigma_t f_c I},$$

or

$$\dot{M} [M_\odot \text{ yr}^{-1}] = \frac{2.33 \times 10^{-7} v_\infty (\text{km s}^{-1}) a (R_\odot) A_p}{(1 + \cos^2 i) f_c I}. \quad (6)$$

We can now estimate \dot{M} by utilizing the observed polarization variability amplitude A_p and orbit inclination $i = 22.5^\circ$ given by Rosu et al. (2023). We used the value of wind velocity $v_\infty = 2335 \text{ km s}^{-1}$ for both components as determined from the combined IUE spectra by Howarth et al. (1997). The fraction of total light $f_c = (1 + 10^{-0.4\Delta M_V})^{-1} = 0.413$ was calculated using $M_{V,p} = -4.17$ and $M_{V,s} = -3.79$, for primary and secondary components respectively, given by Rosu et al. (2023). We have used the plot given by St. -Louis et al. (1988), (Fig. 9 therein) in order to choose the appropriate value of integral $I = 12.3$, which is obtained for $\beta = 0.8$ as suggested by Abbott et al. (1986) and Corcoran (1991) for O-type stars, $\epsilon = R'_i / R_* = 1.0$ (assuming that the scattering envelope is optically thin), where R'_i is measured with respect to the center of the primary star, and $a/R_* = 2.1$ with the values of $a_1 \sin i = 5.66 R_\odot$, and $R_* = 7.0 R_\odot$ (primary component) given by Rosu et al. (2023). The obtained mass-loss rates are $2.5 \times 10^{-7} M_\odot \text{ yr}^{-1}$, $2.0 \times 10^{-7} M_\odot \text{ yr}^{-1}$, and $1.7 \times 10^{-7} M_\odot \text{ yr}^{-1}$ for B , V , and R passbands respectively. It is to be noted that the mass loss rate derived from Eq. 6 is per one (primary) star, and to get the mass loss rate from the whole system consisting of nearly identical components, this value must be doubled. Our estimation of \dot{M} is in good agreement with the previously derived mass-loss rate of $\dot{M} = 2.24 \times 10^{-7} M_\odot \text{ yr}^{-1}$ published by Chlebowski & Garmy (1991).

4. Conclusions

Our comprehensive polarimetric study of the O+O spectral type binary HD 165052 has clearly revealed the presence of the periodic polarization variability. Our period search unambiguously determined the orbital period value of 2.95510d. This value is in good agreement with the previously determined values of the orbital period 2.95510d Arias et al. (2002) and 2.95515d Linder et al. (2007). The most plausible mechanism of polarization variability is the Thomson scattering of light in the interacting stellar winds. Our polarimetry of the field stars in the near vicinity of HD 165052 revealed complex and strongly non-uniform pattern of interstellar polarization in the cluster NGC 6530. Our multi-wavelengths observations show that in addition to variations of dust particles density and orientations, variation in particles size and composition may occur.

As we have found, polarization variability in HD 165052 is dominated by the second harmonics of the orbital period. This indicates a nearly symmetric scattering material geometry and a high concentration of light-scattering material toward the orbital plane. Based on a refined Fourier fit, we derived the average values of the orbital parameters: orbital inclination $i = 55^\circ + 5^\circ / -55^\circ$, and $\Omega = 148^\circ (328^\circ) + 20^\circ / -22^\circ$, averaged over the B , V , and R passbands. The direction of orbital motion in the sky is clockwise. Using the values of polarization periodic variability amplitude, we estimated the total mass-loss rate of the binary system as $4.0 \times 10^{-7} M_\odot \text{yr}^{-1}$.

We must note, that BME analytic solution does not yield intricate insights into the detailed spatial distribution of the light scattering material. Numerical modeling offers a viable alternative, accounting for component sizes, their separation, and relevant scattering scenarios. This study is a part of our series of investigation of variable linear polarization arising in early-type binary systems. In our future paper in this series, we will present the results of applying of our numerical scattering code modeling on polarization data acquired for AO Cas, DH Cep, and HD 165052 binary systems.

Acknowledgements. This work was supported by the ERC Advanced Grant Hot-Mol ERC-2011-AdG-291659 (www.hotmol.eu). Dipol-2 was built in the cooperation between the University of Turku, Finland, and the Kiepenheuer Institut für Sonnenphysik, Germany, with the support by the Leibniz Association grant SAW-2011-KIS-7. We are grateful to the Institute for Astronomy, University of Hawaii for the observing time allocated for us on the T60 telescope at the Haleakalā Observatory. All raw data and calibrations images are available on request from the authors.

References

Abbott, D. C., Beiging, J. H., Churchwell, E., & Torres, A. V. 1986, *ApJ*, 303, 239
 Abdul Qadir, Y., Berdyugin, A. V., Piirola, V., Sakanoi, T., & Kagitani, M. 2023a, *A&A*, 670, A176
 Abdul Qadir, Y., Berdyugin, A. V., Piirola, V., Sakanoi, T., & Kagitani, M. 2023b, *A&A*, 677, A75
 Arias, J. I., Morrell, N. I., Barbá, R. H., et al. 2002, *MNRAS*, 333, 202
 Aspin, C., Simmons, J. F. L., & Brown, J. C. 1981, *MNRAS*, 194, 283
 Berdyugin, A., Piirola, V., Sadegi, S., et al. 2016, *A&A*, 591, A92
 Brown, J. C., McLean, I. S., & Emslie, A. G. 1978, *A&A*, 68, 415
 Chlebowski, T. & Garmany, C. D. 1991, *ApJ*, 368, 241
 Corcoran, M. F. 1991, *ApJ*, 366, 308
 Damiani, F., Prisinzano, L., Micela, G., & Sciortino, S. 2006, *A&A*, 459, 477
 Drissen, L., Lamontagne, R., Moffat, A. F. J., Bastien, P., & Seguin, M. 1986, *ApJ*, 304, 188
 Ferrero, G., Gamen, R., Benvenuto, O., & Fernández-Lajús, E. 2013, *MNRAS*, 433, 1300
 Gaia Collaboration, Brown, A. G. A., Vallenari, A., et al. 2021, *A&A*, 649, A1
 Hogg, D. W. & Foreman-Mackey, D. 2018, *ApJS*, 236, 11

Howarth, I. D., Siebert, K. W., Hussain, G. A. J., & Prinja, R. K. 1997, *MNRAS*, 284, 265
 Kosenkov, I. A. & Veledina, A. 2018, *MNRAS*, 478, 4710
 Linder, N., Rauw, G., Sana, H., De Becker, M., & Gosset, E. 2007, *A&A*, 474, 193
 Lomb, N. R. 1976, *Ap&SS*, 39, 447
 Manset, N. & Bastien, P. 2000, *AJ*, 120, 413
 Morrison, N. D. & Conti, P. S. 1978, *ApJ*, 224, 558
 Piirola, V., Berdyugin, A., & Berdyugina, S. 2014, in Society of Photo-Optical Instrumentation Engineers (SPIE) Conference Series, Vol. 9147, Ground-based and Airborne Instrumentation for Astronomy V, ed. S. K. Ramsay, I. S. McLean, & H. Takami, 91478I
 Piirola, V., Berdyugin, A., Frisch, P. C., et al. 2020, *A&A*, 635, A46
 Piirola, V., Kosenkov, I. A., Berdyugin, A. V., Berdyugina, S. V., & Poutanen, J. 2021, *AJ*, 161, 20
 Price-Whelan, A., Crawford, S., Sipocz, B., et al. 2018, *Astropy/Astropy-V2.0-Paper: Final Draft*, Zenodo
 Rosu, S., Quintero, E. A., Rauw, G., & Eenens, P. 2023, *MNRAS*, 521, 2988
 Scargle, J. D. 1982, *ApJ*, 263, 835
 Schmidt, G. D., Elston, R., & Lupie, O. L. 1992, *AJ*, 104, 1563
 Shannon, C. E. 1949, *IEEE Proceedings*, 37, 10
 Simmons, J. F. L., Aspin, C., & Brown, J. C. 1982, *MNRAS*, 198, 45
 St.-Louis, N., Moffat, A. F. J., Drissen, L., Bastien, P., & Robert, C. 1988, *ApJ*, 330, 286
 Stickland, D. J., Lloyd, C., & Koch, R. H. 1997, *The Observatory*, 117, 295
 Sung, H., Chun, M.-Y., & Bessell, M. S. 2000, *AJ*, 120, 333
 Suveges, M. 2012, in Seventh Conference on Astronomical Data Analysis, ed. J.-L. Starck & C. Surace, 16
 Topasna, G. A., Jones, R. H., & Kaltcheva, N. T. 2020, *PASP*, 132, 044301
 VanderPlas, J. T. 2018, *ApJS*, 236, 16
 Wolinski, K. G. & Dolan, J. F. 1994, *MNRAS*, 267, 5

Appendix A: Tables

Table A.1: Log of polarimetric observations for HD 165052.

Date	MJD	T_{exp} [s]	N_{obs}	Telescope
2012-07-28	56136.43	640	64	KVA
2012-07-30	56138.44	640	64	KVA
2012-07-31	56139.44	640	64	KVA
2012-08-01	56140.42	640	64	KVA
2012-08-06	56145.42	640	64	KVA
2012-08-07	56146.42	640	64	KVA
2012-08-08	56147.43	640	64	KVA
2012-08-27	56166.38	640	64	KVA
2012-08-28	56167.43	640	64	KVA
2012-08-29	56168.36	640	64	KVA
2012-09-03	56173.36	640	64	KVA
2012-09-04	56174.43	640	64	KVA
2012-09-06	56176.44	640	64	KVA
2012-09-09	56179.36	640	64	KVA
2012-09-10	56180.35	640	64	KVA
2012-09-11	56181.35	640	64	KVA
2012-09-13	56183.35	640	64	KVA
2012-09-14	56184.37	640	64	KVA
2012-09-16	56186.35	640	64	KVA
2012-09-18	56188.37	640	64	KVA
2012-09-20	56190.36	640	64	KVA
2012-09-21	56191.35	640	64	KVA
2012-09-22	56192.34	640	64	KVA
2012-09-25	56195.34	640	64	KVA
2012-09-27	56197.35	640	64	KVA
2012-09-30	56200.34	640	64	KVA
2012-10-02	56202.35	640	64	KVA
2012-10-03	56203.34	640	64	KVA
2012-10-06	56206.33	640	64	KVA
2012-10-08	56208.34	640	64	KVA
2012-10-10	56210.33	640	64	KVA
2012-10-12	56212.33	640	64	KVA
2015-05-14	57156.09	640	64	T60
2015-05-15	57157.06	640	64	T60
2015-05-19	57161.04	640	64	T60
2015-05-19	57161.99	640	56	T60
2015-05-21	57163.98	640	64	T60
2015-05-22	57164.98	640	64	T60
2015-08-11	57245.76	480	48	T60
2015-08-12	57246.74	640	64	T60
2015-08-22	57256.80	640	64	T60
2016-04-21	57499.01	480	48	T60
2016-04-23	57501.03	640	64	T60
2016-04-25	57503.03	640	64	T60
2016-04-26	57504.01	640	64	T60
2023-04-08	60042.08	640	64	T60
2023-04-10	60044.04	640	64	T60
2023-04-11	60045.04	640	64	T60
2023-04-16	60050.06	640	64	T60
2023-04-16	60050.97	640	64	T60
2023-04-17	60051.97	640	64	T60
2023-04-18	60052.97	640	64	T60
2023-04-24	60058.03	640	64	T60
2023-04-24	60058.96	800	80	T60

2023-04-25	60059.95	640	64	T60
2023-05-01	60065.04	640	64	T60
2023-05-02	60066.96	640	64	T60
2023-05-03	60067.96	640	64	T60
2023-05-05	60069.92	640	64	T60
2023-05-07	60071.02	150	15	T60
2023-05-08	60072.04	640	64	T60
2023-05-08	60072.94	640	64	T60
2023-05-09	60073.92	640	64	T60
2023-05-10	60074.91	640	64	T60
2023-05-12	60076.90	640	64	T60
2023-05-13	60077.90	640	64	T60
2023-05-15	60079.03	580	58	T60
2023-05-15	60079.89	640	64	T60

Table A.2: Average polarization degrees (P), and polarization angles (θ) of highly polarized stars.

Star	Filter	P [%]	θ [deg]	Ref.
HD 204827	B	5.789 ± 0.011	57.79 ± 0.02	[1]
	V	5.602 ± 0.019	58.33 ± 0.02	[1]
	R	5.079 ± 0.011	59.21 ± 0.02	[1]
HD 25443	B	5.232 ± 0.092	134.28 ± 0.51	[2]
	V	5.127 ± 0.061	134.2 ± 0.34	[2]
	R	4.734 ± 0.045	133.65 ± 0.28	[2]

References. (1) Piirola et al. (2021); (2) Schmidt et al. (1992).

Table A.3: Numbers, Identifiers, coordinates, parallaxes, distance, reddening magnitudes, polarization degrees, polarization angles, and the number of polarimetric observations of the field stars.

Number	Identifier [Gaia DR3]	Coordinates [J2000d]	Parallax [mas]	Filter	P [%]	θ [deg]	N_{obs}
1	4066065089814336768	271.3059076143, -24.3803046097	0.8970±0.0163	<i>B</i>	0.4510±0.0714	63.6±4.5	48
				<i>V</i>	0.4670±0.0505	67.1±3.1	48
				<i>R</i>	0.5632±0.0433	68.9±2.2	48
2	4066053132629912320	271.3179724764, -24.4198101995	0.6584±0.0428	<i>B</i>	2.3768±0.2326	60.8±2.8	20
				<i>V</i>	2.2920±0.1523	60.0±1.9	20
				<i>R</i>	2.3349±0.0878	61.1±1.1	20
3	4066051522042471680	271.2812461348, -24.4997570914	0.8377±0.0202	<i>B</i>	0.5098±0.0216	50.6±1.2	15
				<i>V</i>	0.3841±0.0353	53.9±2.6	15
				<i>R</i>	0.4584±0.0173	53.0±1.1	15
4	4066052617233631488	271.2459306023, -24.4564830252	0.8165±0.0209	<i>B</i>	0.5116±0.0135	9.3±0.8	16
				<i>V</i>	0.5845±0.0208	8.4±1.0	16
				<i>R</i>	0.5502±0.0188	6.0±1.0	16
5	4066051281524301696	271.3092838328, -24.5108898514	0.8910±0.0145	<i>B</i>	0.3849±0.0668	65.7±4.9	16
				<i>V</i>	0.2134±0.0565	57.4±7.4	16
				<i>R</i>	0.2802±0.0298	54.7±3.0	16
6	4066064540063670016	271.2674438044, -24.4193396203	0.8975±0.0155	<i>B</i>	0.6153±0.0410	60.7±1.9	16
				<i>V</i>	0.6890±0.0440	58.2±1.8	16
				<i>R</i>	0.6409±0.0289	66.8±1.3	16
7	4066064819261901440	271.2344044218, -24.4010174976	0.7160±0.0171	<i>B</i>	1.0775±0.0297	172.3±0.8	14
				<i>V</i>	0.7497±0.0473	175.1±1.8	14
				<i>R</i>	1.2141±0.0249	172.3±0.6	14
8	4066053201350041088	271.2972066384, -24.4103922466	0.8567±0.0348	<i>B</i>	0.1635±0.1177	5.9±17.9	15
				<i>V</i>	0.3246±0.0435	14.8±3.8	15
				<i>R</i>	0.3290±0.0466	7.7±4.0	15
9	4066052995190959360	271.3533088425, -24.4168530036	0.8305±0.0245	<i>B</i>	0.3899±0.1245	64.7±8.9	16
				<i>V</i>	1.1575±0.2386	46.8±5.8	16
				<i>R</i>	0.9917±0.1533	48.4±4.4	16
10	4066055095455592576	271.3894338404, -24.3548659296	0.8200±0.0221	<i>B</i>	0.5685±0.0469	58.6±2.4	16
				<i>V</i>	0.5259±0.0372	65.5±2.0	16
				<i>R</i>	0.4354±0.0186	61.9±1.2	16
11	4066066979600006656	271.3191660725, -24.3315901481	0.8094±0.0163	<i>B</i>	0.3561±0.0558	14.5±4.5	16
				<i>V</i>	0.3576±0.0446	179.8±3.6	16
				<i>R</i>	0.4983±0.0391	11.7±2.2	16
12	4066066498563609344	271.2211466119, -24.3244706110	0.6556±0.0366	<i>B</i>	0.4807±0.0273	66.7±1.6	16
				<i>V</i>	0.4835±0.0299	65.8±1.8	16
				<i>R</i>	0.5850±0.0229	66.7±1.1	16
13	4066053755426343936	271.3864322875, -24.4088938655	0.6348±0.0190	<i>B</i>	2.4666±0.0888	34.2±1.0	24
				<i>V</i>	2.5907±0.0931	30.7±1.0	24
				<i>R</i>	2.3911±0.0586	29.3±0.7	24
14	4066066429849761408	271.2238606428, -24.3248992994	0.8021±0.0155	<i>B</i>	0.6839±0.1104	57.0±4.6	16
				<i>V</i>	0.9438±0.0612	61.3±1.9	16
				<i>R</i>	0.8156±0.0709	63.1±2.5	16
15	4066064814936438400	271.2417881244, -24.4057311137	0.6839±0.0178	<i>B</i>	0.6114±0.1421	6.5±6.5	16
				<i>V</i>	0.6839±0.0652	4.9±2.7	16
				<i>R</i>	0.6443±0.0272	6.4±1.2	16
16	4066052209237880576	271.3439872723, -24.4397975463	0.9004±0.0164	<i>B</i>	2.7302±0.1238	2.0±1.3	14
				<i>V</i>	2.8448±0.0340	174.7±0.3	14
				<i>R</i>	3.0119±0.0259	175.6±0.2	14
17	4065970398702755968	271.1991211204, -24.4733855530	0.8158±0.0181	<i>B</i>	0.2941±0.0225	75.6±2.2	19
				<i>V</i>	0.2673±0.0344	75.2±3.7	19
				<i>R</i>	0.1920±0.0232	78.7±3.4	19
18	4066064643142852224	271.2108418248, -24.4283694408	0.7632±0.0153	<i>B</i>	2.3064±0.0343	159.9±0.4	24
				<i>V</i>	2.6995±0.0497	159.3±0.5	24
				<i>R</i>	2.7587±0.0269	159.0±0.3	24
19	4066066120606487552	271.2389172227, -24.3468236972	0.5473±0.0307	<i>B</i>	4.1504±0.1093	13.7±0.8	24
				<i>V</i>	3.5982±0.0123	6.0±0.1	24
				<i>R</i>	3.9686±0.0096	9.7±0.1	24
20	4066052793353449856	271.2741311882,	0.8720±0.0195	<i>B</i>	0.9895±0.2411	62.2±6.8	20
				<i>V</i>	0.3237±0.1837	71.2±14.8	20

Number	Identifier [Gaia DR3]	Coordinates [J2000d]	Parallax [mas]	Filter	P [%]	θ [deg]	N_{obs}
		-24.4239033454		R	0.5309±0.0684	72.4±3.7	20
21	4066052758993708032	271.2639480402,	0.8527±0.0207	B	0.6156±0.1215	58.4±5.6	20
		-24.4454711067		V	0.2688±0.1223	49.9±12.2	20
22	4066065712615114880	271.2143725965,	0.6601±0.0266	R	0.6073±0.1010	54.4±4.7	20
		-24.3675817201		B	2.3927±0.4187	161.2±5.0	20
23	4066066743407427328	271.3469938928,	0.8506±0.0175	V	1.7056±0.1441	162.2±2.4	20
		-24.3345472232		R	2.5474±0.0729	166.2±0.8	20
24	4066052862072911104	271.3368141244,	0.8389±0.0244	B	0.0698±0.0579	174.6±19.8	20
		-24.4427979636		V	0.4647±0.0979	33.1±5.9	20
				R	1.1782±0.1597	169.7±3.9	20
				B	2.0197±0.3458	132.1±4.9	16
				V	2.8932±0.2451	39.4±2.4	16
				R	2.8648±0.1942	47.7±1.9	16

Appendix B: Formulae

The formulae given by Drissen et al. (1986) are given in this section. For the orbital inclination (i):

$$\begin{aligned} \left(\frac{1 - \cos i}{1 + \cos i}\right)^4 &= \frac{(u_1 + q_2)^2 + (u_2 - q_1)^2}{(u_2 + q_1)^2 + (u_1 - q_2)^2} \\ &= \frac{(u_3 + q_4)^2 + (u_4 - q_3)^2}{(u_4 + q_3)^2 + (u_3 - q_4)^2}. \end{aligned} \quad (\text{B.1})$$

Longitude of ascending node (Ω) can be computed using the following:

$$\tan \Omega = \frac{A + B}{C + D} = \frac{C - D}{A - B}, \quad (\text{B.2})$$

where,

$$\begin{aligned} A &= \frac{u_4 - q_3}{(1 - \cos i)^2}, & B &= \frac{u_4 + q_3}{(1 + \cos i)^2}, \\ C &= \frac{q_4 - u_3}{(1 + \cos i)^2}, & D &= \frac{u_3 + q_4}{(1 - \cos i)^2}. \end{aligned} \quad (\text{B.3})$$

The following formulae can be used to derive A_q and A_u :

$$A_q = \left(\frac{q_3^2 + q_4^2}{q_1^2 + q_2^2}\right)^{\frac{1}{2}} \left(\frac{J^2 + K^2}{N^2 + R^2}\right)^{\frac{1}{2}}, \quad A_u = \left(\frac{u_3^2 + u_4^2}{u_1^2 + u_2^2}\right)^{\frac{1}{2}} \left(\frac{E^2 + F^2}{L^2 + M^2}\right)^{\frac{1}{2}}, \quad (\text{B.4})$$

where,

$$\begin{aligned} E &= \sin 2i \cos \Omega, & F &= 2 \sin i \sin \Omega, & J &= \sin 2i \sin \Omega, & K &= 2 \sin i \cos \Omega, \\ L &= (1 + \cos^2 i) \cos \Omega, & M &= 2 \cos i \sin \Omega, & N &= (1 + \cos^2 i) \sin \Omega, & R &= 2 \cos i \cos \Omega. \end{aligned} \quad (\text{B.5})$$

We can compute the moment $\tau_0 H$ as follows:

$$\tau_0 H = \left(\frac{q_3^2 + q_4^2}{L^2 + M^2}\right)^{\frac{1}{2}} = \left(\frac{u_3^2 + u_4^2}{N^2 + R^2}\right)^{\frac{1}{2}}. \quad (\text{B.6})$$